End-to-end performance of an uplink NB-IoT transmission relayed on a low-altitude UAV platform with Non-Orthogonal Single-Carrier FDMA in the optical wireless backhaul link
Accepted for being Published

Joan Bas · **Alexis A. Dowhuszko**

Abstract A current trend in the evolution of mobile communication networks consists in integrating Non-Terrestrial Networks (NTN) with the Terrestrial ones. One option to implement the NTN part of this hybrid architecture using Unmanned Aerial Vehicles (UAV) that relay the uplink radio signals through optical wireless backhaul links. A good choice for the radio uplink waveform is conventional SC-FDMA, which mitigates the PAPR and enables a longer battery lifetime at the transmitter side. For the optical backhaul link, which is based on low-cost Visible Light Communication (VLC) technology, a non-orthogonal implementation of SC-FDMA is proposed. By doing so, it is possible to improve the end-to-end throughput by reducing the communication bandwidth (to make it fit the LED frequency response), mitigate the effect of light reflections, and increase the energy efficiency in the backhaul link. Since VLC relies on non-coherent IM/DD, the non-orthogonal SC-FDMA waveform must rotate the phase of the IDFT subcarriers, in order to obtain real-valued signal samples at the output. Two strategies for relaying the data in the UAV node are evaluated, namely: *Detect-and-Forward* and *Decode-and-Forward*. The first one recovers the modulation part (*i.e.* partial regeneration), whereas the second one regenerates the transmitted message up to the bit level (*i.e.*, total regeneration). This paper studies the combination of relaying strategy and NB-IoT Modulation and Coding Scheme (MCS) that maximizes the end-to-end throughput at different UAV altitudes.

J. Bas
Av. Karl Friedriech Gauss 6-7, 08860 Castelldefels, Spain
Tel.: +34-93-678910 / Fax: +34-94-678910
E-mail: joan.bas@cttc.es

A. Dowhuszko
Department of Communications and Networking, Aalto University, 02150 Espoo, Finland
Tel.: +358-46-9226015
E-mail: alexis.dowhuszko@aalto.fi

1 Introduction

Contemporary generations of mobile communication systems aim at providing global coverage by integrating Terrestrial Networks with Non-Terrestrial ones [1]. Apart from satellites placed in different Earth orbits, Non-Terrestrial Networks (NTN) can also rely on High-Altitude Platforms (HAPs) and low-altitude Unmanned Aerial Vehicles (UAVs). HAPs operate at an altitude that varies between 8 and $50\,\text{km}$, and maintain a quasi-static position in the stratosphere using solar power [2]. On the other hand, UAVs are usually drones, Remotely Pilot Aircraft System (RPAS), and non-piloted air-crafts whose positions can be changed in a more agile way [3]. Civil regulations limit the maximum altitude of UAV operations below $100\,\text{m}$, in a range that should not exceed a radius of $1\,\text{km}$. When compared to HAPs, UAVs are used for shorter times, permit much rapid deployments due to their higher maneuverability, and are generally equipped with multiple sensors (*e.g.*, optical and multi-spectral cameras, thermal sensors, LIDAR systems, ground penetration radars, lightweight portable radiometers, *etc.*) As a result, UAVs are used in a plethora of areas related with the Internet-of-Things (IoT), such as agriculture and farming, transportation, medical, disaster and crisis management, energy applications, mobile edge computing and caching to name a few [4]. All these IoT applications have well-known open issues, such as coverage extension, capacity enhancement, and energy consumption constrains [5].

In order to increase the coverage range of UAVs, several approaches have been proposed in the literature. For example, the authors of [6] study the altitude that the UAV should take to maximize the coverage radius, averaging out the channel path loss attenuation that is observed in each case [7]. Note that the higher (lower) is the altitude of the UAV, the better (worse) is the Field-of-View (FOV) and the higher (lower) is the path loss attenuation. Similarly, the use of multiple UAVs as cooperative relays was proposed in [8] to extend the coverage range of the communication system. In this case, the most convenient location of the UAVs was selected to maximize the average rate, considering that the Bit Error Rate (BER) was below a predefined threshold.

Regarding the capacity enhancement of UAV-based communications, the authors of [9] proposed to use UAVs equipped with multiple antennas to increase the data rate in the uplink direction of communication (*i.e.*, from the ground-based terminals to the UAV). Alternatively, the authors of [10] maximized the sum-rate throughput of multiple UAVs by jointly optimizing their trajectories and their transmit powers. In [11], instead of maximizing the sum-rate from ground users to UAVs, it was proposed to maximize the minimum rate of individual links to give a more fair solution.

Towards the optimization of the energy consumed in UAVs, the authors of [12] determined the optimal number of way-points, their positions, and the speed at which the UAV should travel between them, in order to minimize its fuel consumption. Similarly, in [13], it was proposed to reduce the energy consumption of an UAV by optimizing its flight trajectory according to a known scatter distribution. Next, [14] optimized the energy consumption in a swarm of UAVs by developing an scheduling that

minimizes the number of transmissions. The authors of [13] took advantage of the data collection capability of UAVs which, after being broadcast to the users, it was harvest and forwarded to the UAV in half- and full-duplex mode. In [15], the transmission time that minimized the number of re-transmissions was optimized, by taking into account the channel estate information and planned trajectory to reduce the UAV energy consumption. Finally, the authors of [16] developed an algorithm to allocate the bandwidth per cell, which was assigned to the swarm of UAVs according to their demand.

The previously listed solutions enable to enhance the coverage, capacity, and energy consumption of the UAVs. However, all of these solutions assume that the uplink and downlink channels are based on radio communication technologies. An alternative solution could be based on using an optical wireless technology for the backhaul link, such as Visible Light Communications (VLC). Both radio and light signals are electromagnetic waves and, due to that, they propagate at the same speed; however, VLC is a more energy-efficient solution if the same light beam is used simultaneously for two purposes, such as wireless communications and visual signaling of the UAV position. Additionally, state-of-the-art research has not studied the use of different relaying strategies in the UAV, has not considered the reduction of the communication bandwidth in the backhaul link using frequency packing, and has not assessed the gain when adjusting the code rate of the error control coding scheme to optimize the end-to-end throughput.

Toward this regard, this paper focuses on the reverse link of an NB-IoT system, which starts in the ground-based users and ends in the gateway after passing through the intermediate UAV relaying node. Specifically, it is considered that the access link is implemented on RF bands, whereas the backhaul link is implemented using VLC technology.The use of optical bands in the reverse links permits to save energy since LED technology is very energy efficient. Current UAVs have a maximum flight time of 25-30 minutes. So, by resorting to more energy efficient solutions we expect to increase the flight time of UAVs. Furthermore, it can be reused the illumination infrastructure of LEDs for providing additional services such a communications, positioning and even infer the type of obstruction that the communication suffers [17]. According to legal rules UAVs require to visualize the ground station [18]. Consequently, the use of communications based on light for UAVs seems appropriate since they require LoS channels.

The signal transmitted in the radio access link follows the NB-IoT standard, which is based on Single Carrier (SC)-Frequency Division Multiple Access (FDMA) for the NPUSCH in *format 1* [19]. A SC-FDMA waveform has the advantage of minimizing the Peak-to-Average-Power-Ratio (PAPR) and, as result, is effective for extending the battery duration in the transmitter. Since the backhaul link is based on VLC, it can not be taken as reference the baseline SC-FDMA scheme; this is because the flat frequency-response bandwidth of an LED is notably limited, particularly at high transmission powers. Due to that, the precoded DFT remains, but the sub-carriers of the IDFT are overlapped. By doing so, the bandwidth of the resulting non-orthogonal SC-FDMA signal is reduced, enabling to increase the end-to-end throughput and to use low-cost phosphor-converted LEDs in the VLC transmitter. In [20] is also used SC-FDMA for the downlink of VLC communications. However,

they resort to Distributed Frequency Division Multiplexing Access (DFDMA) mapping of the IDFT sub-carriers whereas here it used the Localized Frequency Division Multiple Access (LFDMA) strategy since it is the one used by NB-IoT. Furthermore, LFDMA minimizes the bandwidth in which the DFT precoded signals are spread along the IDFT sub-carriers and so it fits with frequency-sharing strategies.

VLC systems uses Intensity Modulation (IM)/Direct Detection (IM) transmission scheme for communication. Hence, the VLC transmission is non-coherent, and an Hermitian Symmetry property is required to obtain a baseband orthogonal multi-carrier waveform that is real-valued. However, to obtain a non-orthogonal multi-carrier waveform in baseband, it is necessary to add an additional *phase rotation* at the output of the Hermitian Symmetry block, whose coefficients have been derived for the first time in this paper. Finally, two different relaying strategies are considered to forward the information on the UAV, namely *Detect-and-Forward* and *Decode-and-Forward*. In the first case, the symbols of the NB-IoT frame are detected and re-modulated one-by-one in the UAV, whereas in the second case the decoding and re-encoding of the blocks of information is also performed in the UAV before forwarding the information to the gateway. Thus, according to the channel conditions which vary according to the UAV altitude, it will be more convenient to regenerate partially or totally the transmitted signal in the UAV to optimize the end-to-end throughput of the system.

The rest of the paper is organized as follows: Section 2 presents the system model, formulates the channel models for the radio access and VLC backhaul links, and specifies the details of the *Detect-and-Forward* and *Decode-and-Forward* relaying strategies. Section 3 develops the signal processing blocks to obtain the Non-orthogonal SC-FDMA signal, whereas Section 4 shows the results for both UAV relaying strategies in terms of Block Error Rate (BLER) and throughput for different UAV altitudes. Finally, the main outcomes of the paper are summarized in Section 5.

2 System Model

The aim of this paper is to optimize the end-to-end throughput when different Modulation and Coding Schemes (MCS), belonging to the NB-IoT standard, are used to encode the information that IoT devices generate. As shown in Fig. 1, the flow of information in the NB-IoT uplink takes place over two links, known as the radio access link and the optical backhaul link. The relaying node that is placed on the UAV is in charge of adapting the complex-valued signal samples received on the radio access link into real-valued signal samples, which are suitable for IM/DD on the optical backhaul link. Two different relaying strategies are considered in the UAV, namely *Detect-and-Forward* and *Decode-and Forward*. In addition, frequency-sharing is implemented in the optical backhaul link, such that the bandwidth of the signal that modulates in intensity the light beam is reduced to fulfill the electrical passband of the LED transmitter.
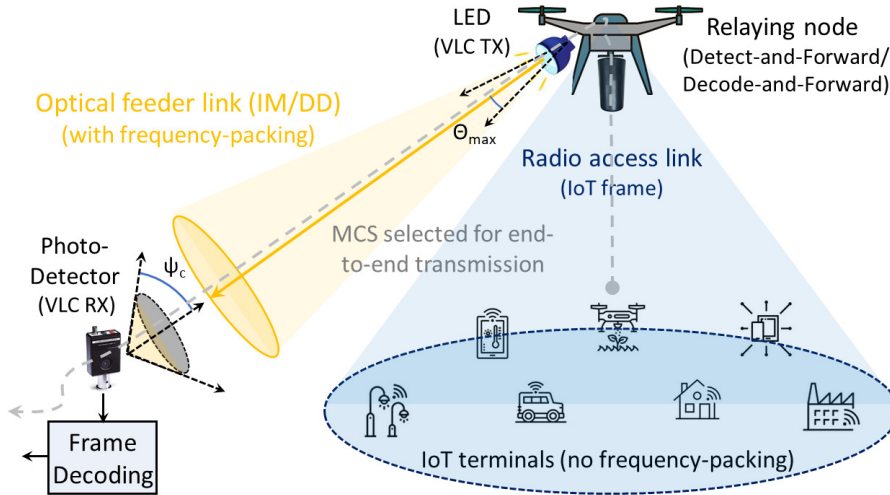
Fig. 1: *Block diagram of a moving cell mounted on a drone that implements NSC-FDMA in the (LED-based) optical feeder link to augment the number of connected NB-IoT devices that can be simultaneously served on the radio access link. The relaying node on the drone implements a Detection-and-Forward/Decode-and-Forward strategy, as well as NSC-FDMA to control the PAPR and minimize the non-linear distortion in the optical feeder link. The NB-IoT Modulation and Coding Scheme (MCS) is selected to mitigate the impact of errors introduced in both radio access and optical feeder parts of the return link.*

2.1 Radio access link of the two-hop NB-IoT relaying architecture

In the access link (*i.e.*, first hop of the uplink flow of information), the IoT-enabled devices and sensors send their data to the intermediate relaying node in the UAV, using for this purpose a NB-IoT block of information that is accommodated on a suitable Radio Frequency (RF) band. In the radio access link, NB-IoT frames consist of 10 radio sub-frames of duration 1 ms each, which span a bandwidth of 180 kHz that defines the minimum resource allocation unit, known as Physical Resource Block (PRB).

The NB-IoT standard defines two possible sub-carrier spacing (Δf). For the case when $\Delta f = 15$ kHz, the data generated by the NB-IoT device is accommodated over $N_s = 12$ subcarriers in a time slot of duration $T_s = 0.5$ ms. On the other hand, for the $\Delta f = 3.75$ kHz case, the data block is placed on $N_s = 48$ subcarriers with $T_s = 2$ ms. In addition, there are two possible transmission strategies, namely single-tone and multi-tone. According to the NB-IoT standard, a single-tone transmission can only be scheduled when $\Delta f = 3.75$ kHz, whereas the multi-tone transmission is possible for both sub-carrier spacing (*i.e.*, for $\Delta f = 3.75$ kHz and 15 KHz).

In the uplink direction of communication, the NB-IoT standard defines three communication channels, namely: *Demodulation Reference Signal* (DMRS), *Narrowband Physical Uplink Shared Channel* (NPUSCH), and *Narrowband Physical Random Access* (NPRACH). The DMRS is used to estimate the channel gains in uplink, the NPUSCH is used to transmit the data/control information, whereas the NPRACH is used to transmit the preambles of the random access procedures. For the sake of simplicity, this paper focuses on the studying of the NPUSCH channel, which can be
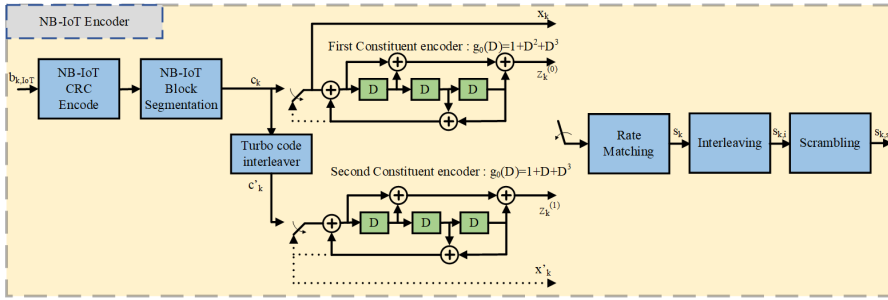
Fig. 2: *Overview of rate $1/3$ tail-biting NB-IoT Turbo coding with rate matching, interleaving, and scrambling that is implemented in the NB-IoT uplink [21].*

configured into *format 1* for payload data and *format 2* for control information (*e.g.*, ARQ signaling). The NPUSCH channel appends a 24-bit CRC to the each block of payload data and, after that, encodes the resulting symbols with a Turbo Code with rate $1/3$, which can be implemented in practice using two encoding polynomials: $g_0 = 1 + D^2 + D^3$ and $g_1 = 1 + D + D^3$ [21]. Next, the encoded data is rate-matched to obtain the target code rate, interleaved, scrambled, QPSK mapped, and finally SC-FDMA modulated. After that, the uplink NB-IoT frame is sent to the UAV. Fig. 2 gives an overview of this processing, which takes place in the NB-IoT uplink.

Regarding the uplink channel model of the UAV, it has been resorted to the one proposed in [22], [23]. Specifically, the semi-urban channel model, which includes the environmental effects (e.g. vegetation, buildings, containers, etc). It does not include atmospheric effects since for legal reasons UAVs have to fly in perfect weather conditions, (*i.e.* no rain, no fog, and no wind) [18]. This is one of the main differences with the channel from satellite communications, which have to be designed to support atmospheric impairments. Another difference is that the variability of the UAV channel with the altitude is much larger than the satellite one. For an altitude of 10m the distribution of the UAV channel follows a Rayleigh one due to the multipath reflection with the ground. On the contrary, at an altitude of 30m and semi-urban channel tends to be a Line of Sight. As result, its channel is modelled with a Ricean distribution with a Ricean factor, K, that depends on the altitude of the UAV [22], [23].

2.2 Optical backhaul link of the two-hop NB-IoT relaying architecture

In the UAV, the NB-IoT SC-FDMA waveform is first regenerated and then forwarded to the gateway. Specifically, this paper considers two possible regenerative structures in the UAV, namely: i) *Detect-and-Forward* and ii) *Decode-and-Forward*.

In *Detect-and-Forward*, the signal received in the first hop is regenerated up to the symbol mapping level of the NB-IoT frame, whereas in *Decode-and-Forward* the NB-IoT block of information is fully regenerated (including Turbo decoding and re-encoding before before forwarding the information). After the regeneration process in the UAV, the blocks of information are modulated using a Non-orthogonal Single-

Carrier Frequency-Division Multiple-Access (NSC-FDMA) strategy that has been adapted to fulfill the IM/DD and low-bandwidth requirements of the optical backhaul link. That is, the baseline SC-FDMA modulation block was adapted to have overlapping in the sub-carriers of the IDFT stage. According to this, the optical backhaul link follows the data mapping, channel encoding, and numerology of the NB-IoT standard. Then the resulting optical NSC-FDMA signal is sent to the gateway via the optical backhaul link and, after being optical-to-electrical converted in the Photodetector (PD) receiver, the signal samples are equalized to remove the Inter-Carrier Interference (ICI) that the use of non-orthogonal subcarrier placement introduce.

Finally, Fig. 3 shows the unified architecture of the two proposed relaying strategies in the UAV. Green boxes with solid lines indicate the signal processing blocks that are needed to implement the *Detect-and-Forward* strategy, whereas the orange boxes with dashed-lines identify the additional blocks that are needed to implement the *Decode-and-Forward* strategy. The details of the corresponding signal models are now presented in the following sections.
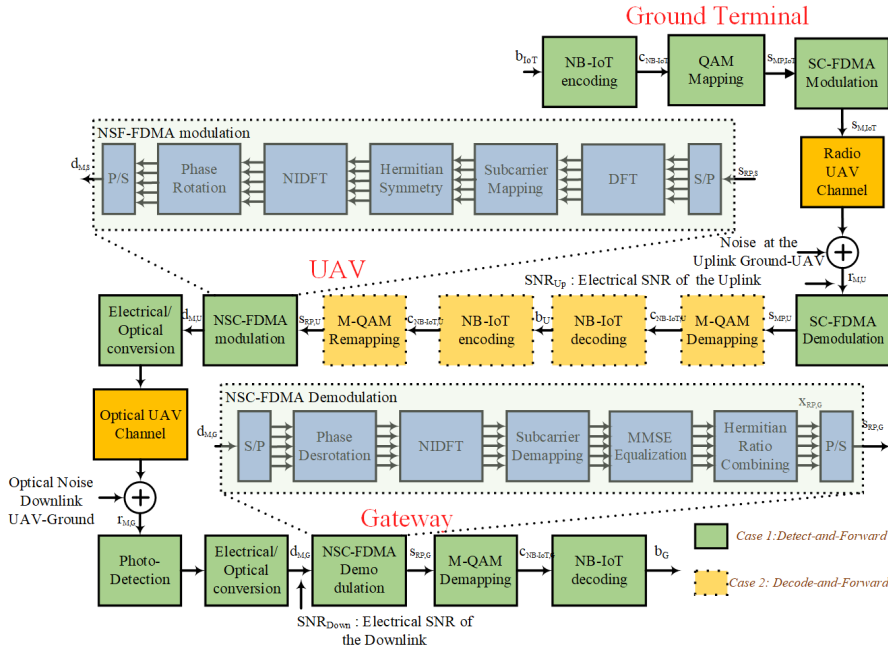

Fig. 3: *Block diagram of the UAV return link for the two relaying configurations under analysis: 1) Detect-and-Forward with NB-IoT (green blocks with solid edges); and 2) Decode-and-Forward with NB-IoT (orange blocks with dotted edges). In blue the sub-blocks that form the NSC-FDMA modulator and demodulator (See Section 3).*

2.3 Relaying architectures for a UAV-based system

In order improve the throughput of contemporary 5G networks, this paper focuses on the use of relaying nodes mounted on UAVs. The use of regenerative payloads has already been considered as an option for NTN in 3GPP standardization [1]. However, apart from the fully regenerative relaying strategy, this paper also studies the performance of a partial regenerative relaying strategy, which detects the QPSK-modulated symbols of the NPUSCH and re-modulates them before forwarding them to the backhaul link. On the contrary, the fully regenerative strategy detects the payload bits after the Turbo decoder, re-encodes them in NB-IoT format, and forwards them in the backhaul link. According to this, they have been named as *Detect-and-Forward* (*i.e.*, partial-regenerative) and *Decode-and-Forward* (*i.e.*, fully-regenerative). In the following subsections, the detail of the corresponding signal models are now presented.

2.3.1 Detect-and-Forward non-regenerative relaying strategy

Let s_{IoT}, h_{ul}, and η_{uav} be the SC-FDMA symbol that the IoT device transmits, the radio channel gain from the NB-IoT terminal to the UAV in uplink, and the complex AWGN in the UAV, respectively. Thus, the n-th SC-FDMA signal sample that is received in the UAV can be written as

$$r_{\mathrm{uav}}[n] = \sqrt{\left(\frac{E_{\mathrm{b}}}{N_0}\right)_{\mathrm{ul}}} h_{\mathrm{ul}}\, s_{\mathrm{IoT}}[n] + \eta_{\mathrm{uav}}[n], \tag{1}$$

where $(E_{\mathrm{b}}/N_0)_{\mathrm{ul}}$ is the energy-per-bit-to-noise-power-spectral-density ratio of the radio access link in uplink. With the aid of these signal samples, the SC-FDMA is demodulated and the QPSK symbols $\widehat{s}_{\mathrm{IoT}}$ are estimated in the UAV. After that, each of these QPSK estimated symbols are re-modulated using the proposed NSC-FDMA scheme. If we consider that the SC-FDMA modulation has in its IDFT stage K subcarriers with overlapping factor δ, then the NSC-FDMA signal samples attain the form

$$d_{\mathrm{IoT}}[n] = \frac{1}{\sqrt{N}} \sum_{k=0}^{K-1} x_{\mathrm{IoT}}[k]\, \exp\left(\mathrm{j}\frac{2\pi\, k\, n\, (1-\delta)}{K}\right), \tag{2}$$

where

$$x_{\mathrm{IoT}}[k] = \frac{1}{\sqrt{M}} \sum_{l=0}^{M-1} \widehat{s}_{\mathrm{IoT}}[l]\, \exp\left(-\mathrm{j}\frac{2\pi\, l\, k}{M}\right) \tag{3}$$

is the signal at the output of the DFT of the NSC-FDMA system, and $\widehat{s}_{\mathrm{IoT}}$ is the SC-FDMA modulated symbol. However, the resulting NSC-FDMA signal samples from (2) are complex-valued, and they should become real-valued in order to fulfill the requirement of an optical transmission strategy on a (non-coherent) IM/DD link. Toward this regard, it is possible to convert the complex-values NSC-FDMA signal samples to a real-valued one by rotating the elements of symbol d_{IoT} as follows:

$$\widetilde{d}_{\mathrm{IoT}}[n] = d_{\mathrm{IoT}}[n]\, \exp\left(-\mathrm{j}\,\pi\, n\, (1-\delta)\right). \tag{4}$$

Table 1: Gray mapping for the QPSK modulation symbols.

QPSK symbols	Binary representation $(b_0 \mid b_1)$	Constellation point
s_0	$(0 \mid 0)$	$(-1-j)/\sqrt{2}$
s_1	$(0 \mid 1)$	$(-1+j)/\sqrt{2}$
s_2	$(1 \mid 1)$	$(1+j)/\sqrt{2}$
s_3	$(1 \mid 0)$	$(1-j)/\sqrt{2}$

Section 3 provides the mathematical framework that determines the rotation factor that converts the complex-valued NSC-FDMA signal samples into real-valued ones. After rotating the NSC-FDMA signal samples, a Digital-to-Analog (D/A) conversion is performed, and the continuous time-domain signal $\widetilde{d}_{\mathrm{IoT}}(t)$ is used to modulate in intensity the light beam emitted by the LED which, in case of polarizing the LED in its linear-response region, attains the form

$$v_{\mathrm{o}}(t) = v_{\mathrm{B}} + \beta \left(\frac{\widetilde{d}_{\mathrm{IoT}}(t)}{\sqrt{\mathbb{E}\{|\widetilde{d}_{\mathrm{IoT}}(t)|^2\}}} \right), \tag{5}$$

where the symbol $\mathbb{E}\{\}$ denotes the statistical expectation, v_{B} represents the constant light intensity level (proportional to the DC-offset) and β is the intensity modulation index. Next, the optical NSC-FDMA is forwarded to the gateway via the optical feeder link. In the receiver side, the PD converts the received optical signal into electrical, *i.e.*,

$$\widetilde{r}_{\mathrm{gw}}[n] = \sqrt{\left(\frac{E_{\mathrm{b}}}{N_0} \right)_{\mathrm{dl}}} \, h_{\mathrm{o,dl}} \, \widetilde{d}_{\mathrm{IoT}}[n] + \eta_{\mathrm{gw}}[n] \tag{6}$$

where $(E_{\mathrm{b}}/N_0)_{\mathrm{dl}}$ is the equivalent energy-per-bit-to-noise-power-spectral density ratio of the optical backhaul link in downlink, $h_{\mathrm{o,dl}}$ is the equivalent channel gain response of the optical feeder link, and η_{gw} is real-valued AWGN noise samples in the gateway. After that, the inverse phase rotation procedure is performed to convert the real-valued NSC-FDMA signal samples into complex-valued signal samples using

$$r_{\mathrm{gw}}[n] = \widetilde{r}_{\mathrm{gw}}[n] \, \exp\left(\mathrm{j}\,\pi\,n\,(1-\delta) \right). \tag{7}$$

Then, the rotated NSC-FDMA symbols from (7) are MMSE-equalized to remove the ICI that the use of non-orthogonal subcarriers generate and, after that, the QPSK symbols are detected and combined to exploit the Hermitian Symmetric structure added in transmission to make the signal samples real-valued (see Section 3.2 for further details). After that, the Log-Likelihood-Ratios (LLRs) for the two bits of the QPSK gray-mapped symbols are determined, *i.e.*, $\mathrm{LLR}_{\mathrm{b}_0}$ and $\mathrm{LLR}_{\mathrm{b}_1}$. Towards this regard, Table 1 shows the corresponding QPSK gray mapping used in this paper, whereas Table 2 presents the resulting closed form expressions for the LLR coefficients that corresponds for the two bits. There, the term s_{gw} represents the QPSK symbols after the NSC-FDMA stage (see Section 3.2 for more details). Finally, the LLRs are evaluated at the Turbo decoder, to detect the payload bits $\widehat{b}_{\mathrm{IoT,gw}}$ in the gateway.

Table 2: Closed form expressions for the LLR_{b_0} and LLR_{b_1} for the QPSK modulation.

LLR_{b_m}	QPSK
LLR_{b_0}	$2\,\mathrm{Im}\{s_{\mathrm{gw}}\}/\sigma^2_{\eta,\mathrm{gw}}$
LLR_{b_1}	$2\,\mathrm{Re}\{s_{\mathrm{gw}}\}/\sigma^2_{\eta,\mathrm{gw}}$

2.3.2 Decode-and-Forward regenerative relaying strategy

The *Decode-and-Forward* strategy fully regenerates the NB-IoT bits transmitted in uplink. That is, the relaying node mounted in the UAV detects the SC-FDMA symbols, computes the LLRs of the Gray-mapped QPSK symbols (see Table 2), and decode them by resorting to the Turbo-decoder to estimate the transmitted payload bits $\widehat{b}_{\mathrm{IoT,uav}}$. Next, the *Decode-and-Forward* strategy re-encodes the estimated information using the NB-IoT Turbo-encoder, maps the bits into Gray-mapped QPSK symbols $\widehat{s}_{\mathrm{IoT,uav}}$, and modulates the resulting frame to NSC-FDMA format, $\widetilde{d}_{\mathrm{IoT,uav}}$ (see Section 3.1). After that, the electrical-to-optical conversion of the NSC-FDMA waveform is performed, and the resulting signal is transmitted to the gateway via the optical wireless backhaul link. At the receiver side, the NSC-FDMA signal samples are demodulated following the same procedure described in Section 2.3.1 for the *Detect-and-Forward* relaying strategy.

Finally, if it is compared the complexity between the *Detect-and-Forward* and *Decode-and-Forward* relaying strategies, it is observed that this latter strategy requires to implement an additional M-QAM Remapping, NB-IoT encoding, NB-IoT decoding and M-QAM soft demapping (see yellow boxes in Fig.3) respect to the former one. From all these steps, the two blocks that require more computational resources are the NB-IoT decoding and M-QAM demapping. As it is was presented in section 2.1, the NB-IoT waveform of the reverse link encodes the data using Turbo channel coding. The complexity issue of the Turbo decode is related with the input message length, K, i.e. O(K) [24]. In contrast to LDPC decoding, the complexity of Turbo decoders does not depend on the channel code rate since it is not based on parity check matrices. Regarding to the soft demapping step, its complexity depends on the modulation that has been used, O(2^m), being m the number of bits per modulated symbol [25].

2.4 Optical wireless channel model for the backhaul link (UAV-to-Gateway)

Let us assume that a Phosphor-Converted (PC)-LED is placed on the moving relaying station (UAV) and, after the addition of a concentration lens in the VLC transmitter, the light beam that is generated can be modeled as a Lambertian radiation pattern; then, the DC gain of the optical channel between the LED transmitter and the PD receiver becomes [26]

$$H_{\mathrm{led,pd}}^{\mathrm{dir}}(0) = \begin{cases} \frac{(m+1)A_{\mathrm{pd}}}{2\pi d_1^2}\cos^m(\phi_1)\cos(\psi_1), & 0 \leq \psi_1 \leq \Psi_{\mathrm{c}}, \\ 0, & \psi_1 > \Psi_{\mathrm{c}}, \end{cases} \tag{8}$$

where m is the Lambert index of the PC-LED, A_{pd} [m^2] is the physical area of the PD, ϕ_1 [rad] and ψ_1 [rad] are the angle of irradiance and incidence of the VLC link, respectively, d_1 [m] is the distance between transmitter and receiver, and Ψ_{c} [rad] is the FOV semi-angle of the PD. In practice, the Lambert index of the optical feeder link can be computed from $m = -1/\log_2\big[\cos(\theta_{\max})\big]$, where $\theta_{\max}$ [rad] defines the source radiation semi-angle at half power of the PC-LED.

The spectral optical power of the light that reaches the PD at wavelength λ is

$$p_{\mathrm{o,pd}}^{\mathrm{dir}}(\lambda) = P_{\mathrm{led}}\, H_{\mathrm{led,pd}}^{\mathrm{dir}}(0)\, S_{\mathrm{o}}^{(\mathrm{w})}(\lambda), \tag{9}$$

where P_{led} [W] and $S_{\mathrm{o}}^{(\mathrm{b})}(\lambda)$ are the total radiant power and spectral power distribution of the PC-LED, respectively.

The DC current at the output of the PD is given by

$$i_{\mathrm{pd}}^{\mathrm{dir}}(0) = \int_{\lambda_{\mathrm{l}}}^{\lambda_{\mathrm{u}}} p_{\mathrm{o,pd}}^{(\mathrm{in})\mathrm{dir}}(\lambda)\, \mathrm{R}_{\mathrm{pd}}(\lambda)\, f_{\mathrm{o}}(\lambda)\, d\lambda, \tag{10}$$

where $\mathrm{R}_{\mathrm{pd}}(\lambda)$ [A/W] is the responsivity of the PD and $f_{\mathrm{o}}(\lambda)$ is the transmittance of the optical passband filter of the VLC receiver with lower (λ_{l}) and upper (λ_{u}) cutoff wavelengths, respectively. The sun light and artificial light, as well as the instantaneous power of the data-carrying signal that reaches the PD, generate shot noise with Root Mean Square (RMS) value v_{n} that is added to the thermal noise that the Transimpedance Amplifier (TIA) with gain G_{tia} embedded into the PD introduces.

Based on the previously listed considerations, it is possible to show the SNR at the output of the PD attains the form

$$\Gamma_{\mathrm{pd}}(0) = \left|\big(i_{\mathrm{pd}}^{\mathrm{dir}}(0)\, G_{\mathrm{tia}}\big)/v_{\mathrm{n}}\right|^2. \tag{11}$$

Without loss of generality, we assume that the optical signal that modulates the intensity of the LED fits in the electrical passband of the VLC receiver, such that SNR in all the frequency subcarriers is the same regardless the index of the subcarrier.

3 Non-Orthogonal SC-FDMA Modulator and Demodulator

As explained before, the electrical bandwidth at which an LED shows a flat frequency-response is limited, particularly at high optical transmission powers. Therefore, the use of multi-carrier transmission schemes that overlap the subcarriers enable to fulfill this LED bandwidth limitation constraint, particularly when the DC-bias current and the intensity modulation index β is high. Moreover, VLC uses (non-coherent) IM/DD transmission schemes, which in practice demand that the multi-carrier modulation scheme over the VLC link should verify the Hermitian Symmetric requirement to obtain a sequence of real-valued signal samples, such as in DCO-OFDM and ACO-OFDM [27]. This constraint is also applicable for the proposed NSC-FDMA modulation. However, the output of the NSC-FDMA system is complex-valued, even when the input vector to the IDFT block is Hermitian Symmetric. So, it is necessary to manipulate the NSC-FDMA signal to become real-valued, following the procedure
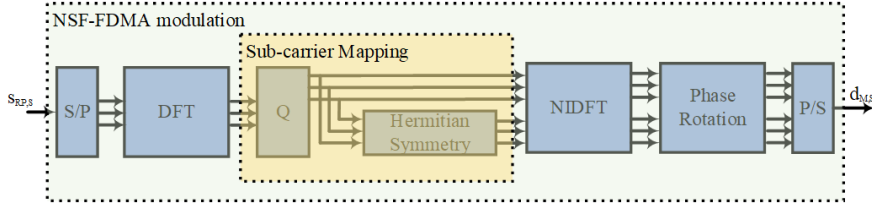
Fig. 4: *Block diagram of the NSC-FDMA modulator to be placed in the UAV.*

that is detailed in Section 3.1. Regarding the demodulation of the NSC-FDMA wave-form, the procedure is similar to the one applied to recover the SC-FDMA signal, but with the addition of an equalizer that removes the ICI that is created by overlapping the subcarriers in the IDFT block of the transmitter (see Section 3.2 for more details). In the following sections, the details of the NSC-FDMA modulation and demodulation procedures are presented in detail.

3.1 Non-Orthogonal SC-FDMA modulation suitable for IM/DD transmission

This section explains the procedure that should be followed to obtain the real-valued signal, suitable for IM/DD transmission, when the subcarriers of the NSC-FDMA waveform use a given frequency overlapping factor. Let us assume that $X[k]$ and $x[n]$ are the k-th input and n-th output subcarriers in the IDFT stage of the NSC-FDMA modulator, δ the subcarrier overlapping factor, and N the total number of subcarriers. Then, the output of the IDFT stage of the NSC-FDMA modulator is given by

$$x[n] = \frac{1}{\sqrt{N}} \sum_{k=0}^{N-1} X[k] \exp\left(\mathrm{j}\frac{2\pi\,k\,n\,(1-\delta)}{N}\right), \tag{12}$$

where the input subcarrier vector $\mathbf{X}$ verifies the Hermitian symmetric constrain, *i.e.*,

$$X[N-k] = X^*[k] \qquad k = 1, 2, \cdots, N/2 - 1, \tag{13}$$

where $(\cdot)^*$ the complex conjugation operation, and the DC subcarriers with index $k=0$ and $-N/2$ are set to zero to avoid any bias from from continuous component.

Separating the terms of the sum in (12) into the two complex conjugate terms normalized by a phase rotating factor, it is possible to see that

$$x[n] = \frac{\exp\left(\mathrm{j}\,\pi\,n\,(1-\delta)\right)}{\sqrt{N}} \left\{ \sum_{k=1}^{N/2-1} X[k] \exp\left(\mathrm{j}\frac{n(1-\delta)(k-N/2)}{N}\right) \right.$$

$$\left. + X^*[k] \exp\left(-\mathrm{j}\frac{2\pi\,n\,(1-\delta)\,(k-N/2)}{N}\right) \right\}. \tag{14}$$

At this point, it is important to notice that the total outcome of the symmetric terms in (14) is a real value, as it is formed by a series of complex conjugated terms. This

is because the input subcarriers in vector $\mathbf{X}$ verify the Hermitian symmetric property. Consequently, (14) can be reformulated in terms of the half of its sub-carriers, *i.e.*,

$$x[n] = \frac{\exp\left(j\,\pi\,n\,(1-\delta)\right)}{\sqrt{N}}\Bigg\{ \sum_{k=1}^{N/2-1} 2\,X_{\mathrm{R}}[k]\,\cos\left(\frac{2\pi\,n\,(1-\delta)(k-N/2)}{N}\right) $$
$$- 2\,X_{\mathrm{I}}[k]\sin\left(-\frac{2\pi\,n\,(1-\delta)(k-N/2)}{N}\right)\Bigg\}, \tag{15}$$

where $X_{\mathrm{R}}[k]$ and $X_{\mathrm{I}}[k]$ are the real and imaginary components of the complex symbol on subcarrier $X[k]$ (*i.e.*, $X[k] = X_{\mathrm{R}}[k] + jX_{\mathrm{I}}[k]$). Then, to achieve a real-valued signal at the IDFT block output, it is necessary to multiply this output by the conjugated value of the rotation factor that normalizes the symmetry of (15). Thus,

$$z[n] = x[n]\exp\left(-j\,\pi\,n\,(1-\delta)\right) \tag{16}$$

is obtained, where $z[n]$ is the rotated output of the IDFT stage of the NSC-FDMA block, which is used modulate the intensity of the LED light in the optical wireless backhaul link (See Fig. 4). Next, (16) can be re-written in a vector notation form as follows:

$$\mathbf{z} = \boldsymbol{\theta}^H\mathbf{x}, \tag{17}$$

where $\boldsymbol{\theta} \in \mathbb{C}^{N\times 1}$ and $\mathbf{x} \in \mathbb{R}^{N\times 1}$ are the vectors that stack the rotation factor and the output of the IDFT, respectively. That is,

$$\boldsymbol{\theta} = \left[1 \cdots \exp\left(j\,\pi\,n\,(1-\delta)\right) \cdots \exp\left(j\,\pi(N-1)\,(1-\delta)\right)\right]^T \tag{18}$$

and $\mathbf{x}^T = \left[x[0] \cdots x[n] \cdots x[N-1]\right]$. The vector at the output of the IDFT can be written as

$$\mathbf{x} = \mathbf{F}_{\mathrm{N},\delta}\,\mathbf{X}, \tag{19}$$

where

$$\mathbf{F}_{\mathrm{N},\delta} = \begin{bmatrix} 1 & 1 & \cdots & 1 \\ 1 & \omega_N & \cdots & \omega_N^{N-1} \\ \vdots & \vdots & \ddots & \vdots \\ 1 & \omega_N^{N-1} & \cdots & \omega_N^{(N-1)(N-1)} \end{bmatrix} \tag{20}$$

represents the non-orthogonal IDFT matrix with N subcarriers with overlapping factor δ, with $\omega = \exp\left(j\frac{2\pi(1-\delta)}{N}\right)$. Note that when $\delta = 0$, the matrix in (20) reduces to the well-known orthogonal IDFT matrix. Regarding the input vector of the IDFT, it can be expressed in terms of the input data to the precoded DFT as

$$\mathbf{X} = \mathbf{Q}\,\mathbf{B}\,\mathbf{s}, \tag{21}$$

where $\mathbf{Q} \in \mathbb{R}^{N\times M}$ is the permutation matrix that implements the change of subcarrier localization during the Hermitian symmetric processing, and its coefficients are given by $Q[N-k,k] = Q[k] = 1$ for $k = 1,\ldots,M$. The matrix $\mathbf{B} \in \mathbb{C}^{M\times 2M}$ stacks
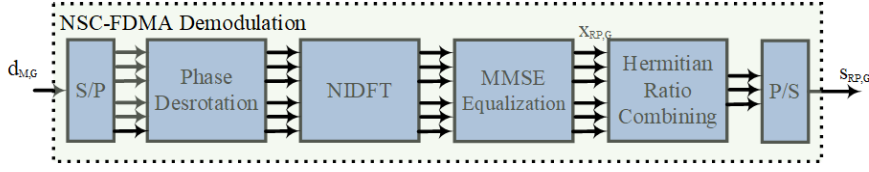
Fig. 5: *Block diagram of the NSC-FDMA demodulator to be placed in the gateway.*

the DFT pre-coded matrix for the QPSK symbols and their conjugated values, *i.e.*, $\mathbf{B} = \left[\mathbf{F_M} \,\middle|\, \mathbf{F_M}^{\mathrm{H}}\right]$, where $\mathbf{F}_M$ is the DFT matrix which attains the form defined in (20) with $\omega = \exp\left(\mathrm{j}\frac{2\pi}{M}\right)$. Finally, $\mathbf{s} \in \mathbf{C}^{2M \times 1}$ is the vector that contains the QPSK symbols detected at the UAV and their conjugated values for being used in the Hermitian transformation, *i.e.*, $\mathbf{s} = \left[\mathbf{s}_{\mathrm{uav}} \,\middle|\, \mathbf{s}_{\mathrm{uav}}^*\right]^T$.

3.2 Equalization of Non-Orthogonal SC-FDMA waveform

As explained before, the use of non-orthogonal SC-FDMA introduces overlapping on the data symbols that are transported on the different subcarrier. Thanks to this approach, the spectral efficiency of the multi-carrier waveform is improved, but the cost that needs to be payed in return is the introduction of ICI that must be mitigated in reception. Towards this regard, in this paper we use MMSE equalization to mitigate the ICI that frequency-sharing introduces in the received signal. For MMSE equalization, it is possible to show that the coefficients of the equalization matrix attain the form

$$\mathbf{A}_{\mathrm{eq}} = \left(\mathbf{G}^{\mathrm{H}}\,\mathbf{G} + \sigma_{\mathrm{bl}}^2\,\mathbf{I}_{2\mathrm{M}}\right)^{-1}\mathbf{G}^{\mathrm{H}}, \tag{22}$$

where $\sigma_{\mathrm{bl},\delta}^2$ is the noise power in the optical backhaul link. This noise power, in order to keep the $E_{\mathrm{b}}/N_{\mathrm{o}}$ of the backhaul link constant when it is applied frequency sharing, it has to fulfill:

$$\sigma_{\mathrm{bl},\delta}^2 = \frac{\sigma_{\mathrm{bl},\delta=0}^2}{1 - \delta} \tag{23}$$

The matrix that generates the NSC-FDMA signal samples is $\mathbf{G} \in \mathbf{C}^{N \times 2M}$. Note that according to the analysis presented in Section 3.1,

$$\mathbf{G} = \mathbf{H}_{\mathrm{bl}}\,\boldsymbol{\theta}^{\mathrm{H}}\,\mathbf{F}_{\mathrm{N},\delta}\,\mathbf{Q}\,\mathbf{B}, \tag{24}$$

where $\mathbf{H}_{\mathrm{bl}} \in \mathbf{R}^{N \times N}$ is the equivalent channel matrix of the optical backhaul link. Then, the equalized MMSE symbols attain the form

$$\mathbf{s}_{\mathrm{mmse}} = \mathbf{A}_{\mathrm{eq}}\,\widetilde{\mathbf{r}}_{\mathrm{gw}}, \qquad \mathbf{s}_{\mathrm{mmse}} \in \mathbb{C}^{2M \times 1}, \tag{25}$$

where $\mathbf{s}_{\mathrm{mmse}} = \left[\mathbf{s}_{\mathrm{gw,mmse}} \,\middle|\, \mathbf{s}_{\mathrm{gw,mmse}}^*\right]^{\mathrm{T}}$ and stacks the estimations of the direct QPSK symbols (subcarriers with positive indexes) and their conjugate complex values (subcarries with negative indexes). Next, in order to estimate the vector of QPSK symbols

that was transmitted, the Hermitian symmetric structure is exploited by applying equal gain combining processing on the received signal samples to obtain

$$\mathbf{s}_{\mathrm{mmse,gw}}[l] = \big(\mathbf{s}_{\mathrm{mmse}}[l] + \mathbf{s}_{\mathrm{mmse}}[l+M]\big)/2, \quad l = 0, \ldots, M-1. \quad (26)$$

Now that the modulation and equalization process of the NSC-FDMA signal has been explained, we are ready to present the simulation results that have been achieved.

4 Simulation results

This section presents the simulation results of the proposed hybrid radio/optical relaying system based on low-altitude UAVs. Toward this regard, Section 4.1 summarizes the details of the simulation scenario, whereas Section 4.2 presents the simulation results and carries out the performance analysis of the different configurations under study. The figures of merit that are used to carry out the performance evaluation are the BLER and throughput for the end-to-end link, starting in the IoT terminals and ending in the gateway. Both *Detect-and-Forward* (Section 2.3.1) and *Decode-and-Forward* (Section 2.3.2) relaying strategies are considered for different UAV altitudes, frequency-overlapping factor in the NSC-FDMA waveform, NB-IoT code rates in the uplink flow of information, and E_{b}/N_0 in the radio access and optical backhaul links.

4.1 Simulation setting

As previously stated, this paper focuses on the uplink flow of information of a NB-IoT system, which is originated in the IoT terminals that use a low-altitude UAV to relay their information towards the IoT gateway. This *reverse* link is formed by two hops.

The first hop, from the IoT-devices to the UAV, is the radio access link that implements SC-FDMA modulation to communicate over the NPUSCH channel. In this channel, the number of subcarriers in the DFT-precoding stage is $M = 12$, the number of sub-carriers of the IDFT stage is $N = 128$, and the modulation scheme is QPSK. The chosen subcarrier spacing is $\Delta f = 15\,\mathrm{kHz}$, with $N_{\mathrm{ru}} = 12$ resource units and multi-tone transmission. For this type of transmission, the number of resource elements is $N_{\mathrm{re}} = 144$, whereas the selected Transport Block Size (TBS) can accommodate up to 256 bits. Then, the resulting code rates that have been used to simulate the uplink transmission for this configuration are $R_{\mathrm{c}} = 0.17, 0.44$, and 0.66 [28].

In the second hop, from the UAV to the gateway, an optical multi-carrier waveform has been considered to modulate the intensity of the VLC link. More precisely, a novel NSC-FDMA scheme has been introduced for the optical backhaul link, and different overlapping factors $\delta = 0\%, 15\%, 25\%$, and 40% have been studied when combined with different code rates in both relaying strategies. The equivalent E_{b}/N_0 for the optical backhaul link was varied from 0 to 20 dB in steps of 1 dB, whereas the E_{b}/N_0 for the radio access link was set to take three possible values (*i.e.*, 10, 15, and 20 dB).

Regarding the uplink radio channel model of UAV has been used the semi-urban one from [22], [23]. More precisely, it follow a Rice distribution, whose mean value and K-factor depends on the altitude that the UAV takes. It has been evaluated for three

different cases, at $H_{\text{uav}} = 10$, 30, and 100 m. Specifically, the values of the Ricean K-factor used in this paper in terms of the altitude of UAV are: $K=\{3(H_{\text{uav}}=10)$ $10(H_{\text{uav}}=30)$ $18(H_{\text{uav}}=100)$ } in dB. Note that the lower (higher) the altitude that the UAV takes, the minor (larger) is the value of the Ricean K-factor. In this situation, the radio access gains tends to a Rayleigh (Line-of-Sight) distribution due to the multipath component increases (vanishes) with the reduction (augment) of the altitude of UAV. Based on this, it is possible to conclude that when the altitude of the UAV grows, the variability of the radio access channel gains reduces, as well as the mean signal power that is received in the UAV.

Concerning the optical backhaul link, an array of Phosphor-Converted (PC) LEDs has been considered as light source of the VLC transmitter (which is also used for visual signaling of the position of the flying UAV). Due to the UAV-based relaying node is designed to work outdoors, under different levels of natural background illumination, the DC-bias point of the PC-LED should be set high enough to enable a deep intensity modulation factor, which is proportional to the AC-signal power that is used to convey the data-carrying signal over the VLC link. A black-silicon photodetector with peak responsivity in the near-infrared region is assumed in the VLC receiver, and a visible light optical filter is considered in reception to eliminate the radiation beyond the optical wavelengths that are emitted by the PC-LED. A concentration lens is also added to the VLC transmitter, such that the radiation semi-angle at half power (θ_{max}) is tuned to provide a trade-off between optical channel gain and link-reliability against the vibrations that the UAV experiences while flying. Finally, we note that the high DC-bias point of the PC-LEDs, as well as the slow time response of the phosphor layer that they have, limit the electrical bandwidth of the VLC transmitter notably. This is the reason why using NSC-FDMA is very important, in order to minimize the impact that the slow response of high-power PC-LEDs create in the end-to-end performance.

All these parameters have been used to configure the settings for measuring the performance of both *Detect-and-Forward* and *Decode-and-Forward* relaying strategies in terms of BLER and Throughput. Finally, the gain that frequency-packing (*i.e.*, $\delta > 0$) provides with respect to the orthogonal case (*i.e.*, $\delta = 0$) has been also studied for both relaying strategies.

4.2 Performance evaluation

This section provides the performance results for the two regenerative architectures under analysis, namely: *Detect-and-Forward*, which partially regenerates the NB-IoT frame until the (QPSK) symbol level, and *Decode-and-Forward*, which totally regenerates the NB-IoT frame, including the decoding and re-encoding of the payload data.

Towards this regard, Fig. 6 and Fig. 7 show the BLER and Throughput for the *Detect-and-Forward* strategy, whereas Fig. 8 and Fig. 9 present the BLER and throughput for the *Decode-and-Forward* strategy. In all these figures, the reference E_{b}/N_0 for the radio access link was set to 15 dB, and the end-to-end performance of the NB-IoT uplink transmission was studied at three different UAV altitudes, namely $H_{\text{uav}} = 10$, 30, and 100 m. The overlapping factors that were considered for the NSC-FDMA

waveform in the optical backhaul link were $\delta = 0\%$, 15%, 25%, and 40%. In all cases, the target BLER was set to 0.01.

From the obtained simulation results, it is possible to observe that at low UAV altitudes, the best choice is to use the *Decode-and-Forward* relaying strategy with low code rates in the NB-IoT frame. For medium to high UAV altitudes, there is no much difference on the BLER when comparing the different configurations. For these UAV altitudes, the use of high code rates in the NB-IoT frame may achieve a BLER lower than the target BLER if the overlapping factor between sub-carriers in the backhaul link is moderate. As expected, the *Decode-and-Forward* relaying strategy provides a better BLER than the *Detect-and-Forward*. However, once a particular configuration attains the desired target BLER, there is no gain in throughput between both configurations, as observed when comparing the curves in Fig. 7 with the ones in Fig. 9.

Note also in Fig.6 and Fig.8 that the higher is the channel coding rate the worse is the BER of the *Detect-and-Forward* and *Decode-and-Forward* systems. However, the larger the altitude, the better is the BER for the same channel coding. The reason is that ther larger the altitude, the higher is the LoS component of the Ricean channel and so, the lower is the variability of the channel. From these figures, it is also interesting to point out that the larger the overlapping factor, the higher is the BER when the channel coding rate increases (*i.e.* less number of protection bits). This is critical for the channel coding rate of R_c=0.66, which only meets the BER target requirement of 10^{-2} for overlapping factors δ lower than 25% and altitudes higher than 30m. This conclusion holds with independence of the non-orthogonal SC-FDMA equalization architecture that be used.

Fig. 10 compares the throughput when using frequency-packing and no-frequency-packing in the backhaul link (*i.e.*, Fig. 10a and Fig. 10b), as well as their corresponding throughput gain (*i.e.*, Fig. 10c and Fig. 10d) for both relaying architectures. Results show that for an E_b/N_0 of $10\,\mathrm{dB}$ and a $10\,\mathrm{m}$ UAV altitude, the use of frequency-packing schemes do not offer gain in throughput. However, if the altitude of the UAV increases to 30 or $100\,\mathrm{m}$, the frequency-packing schemes offer a gain in the order of 18% with respect to no-frequency-packing, when the equivalent E_b/N_0 in the optical backhaul link was larger than $14\,\mathrm{dB}$. Next, if the E_b/N_0 of the radio access link increases to $15\,\mathrm{dB}$, the lower the altitude the larger the gain of the frequency-packing scheme with respect to non-frequency-packing one when using in the *Decode-and-Forward* relaying strategy. In particular, depending on the equivalent E_b/N_0 of the optical access link, throughput gains in the order of 32-68% are attainable. For altitudes between 30 and $100\,\mathrm{m}$, there is an improvement in throughput of around 18% for an equivalent E_b/N_0 of $12\,\mathrm{dB}$ ($14\,\mathrm{dB}$) for the *Decode-and-Forward* (*Detect-and-Forward*) relaying architecture. Finally, for an E_b/N_0 of the radio access link of $20\,\mathrm{dB}$, a UAV altitude of $10\,\mathrm{m}$, and low equivalent E_b/N_0 in the optical backhaul link, the *Detect-and-Forward* relaying strategy offers a larger gain in throughput when using frequency-packing schemes. On the contrary, for an equivalent E_b/N_0 of $12\,\mathrm{dB}$ in the optical backhaul link, the *Detect-and-Forward* relaying scheme provides a larger gain in throughput. For the altitudes of UAV of 30 and $100\,\mathrm{m}$, the throughput gain is around 18% when the E_b/N_0 of the backhaul link is $12\,\mathrm{dB}$ ($18\,\mathrm{dB}$) for the *Decode-and-Forward* (*Detect-and-Forward*) relaying strategy.

(a) $\delta = 0\,\%$ *(no overlapping).*

(b) $\delta = 15\,\%$ *(low overlapping).*

(c) $\delta = 25\,\%$ *(medium overlapping).*
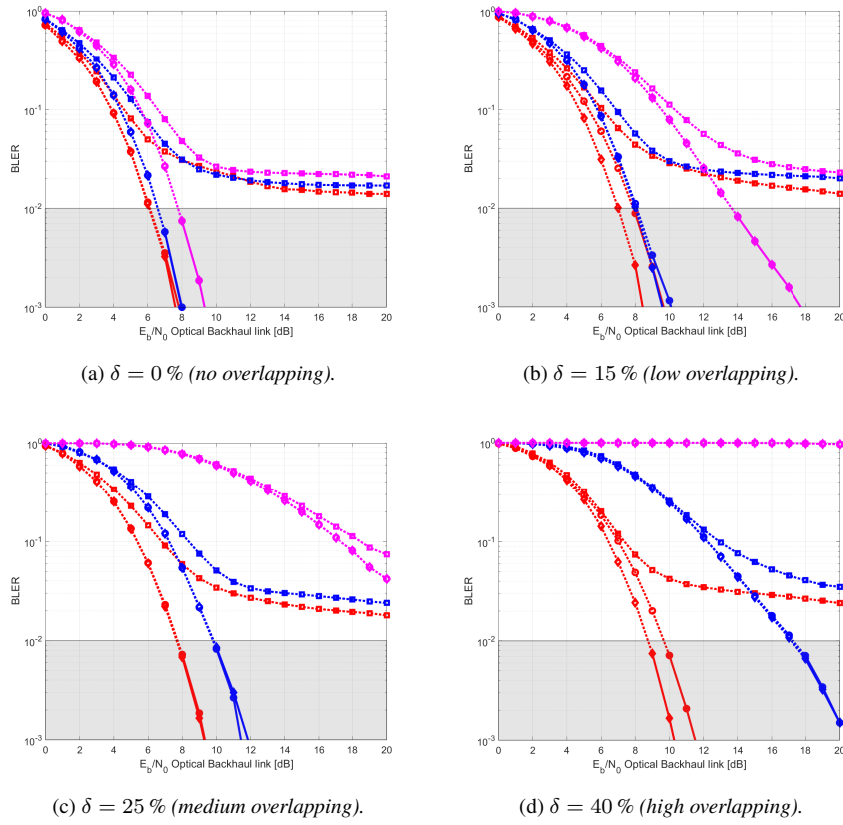
(d) $\delta = 40\,\%$ *(high overlapping).*

Fig. 6: *End-to-end BLER versus equivalent E_{b}/N_0 in the backhaul link for a NB-IoT frame with Detect-and-Forward relaying ($SNR_{\mathrm{al}} = 15\,dB$). NB-IoT code rates: 0.17 (red), 0.44 (blue), 0.67 (magenta). The UAV altitudes are $10\,m$ (square marker), $30\,m$ (circle marker), and $100\,m$ (diamond maker). Solid (dashed) lines with (un)filled markers: BLER 10^{-2} requirement (not) fulfilled.*

5 Conclusions

This paper studied the viability of using different relaying strategies in a UAV with optical backhaul link and radio access link, which aims at connecting NB-IoT devices with an IoT gateway in the uplink direction of communication. The access link was implemented on a RF band and followed the NB-IoT numerology. The optical backhaul link was implemented via VLC technology and used a non-orthogonal SC-FDMA waveform with different overlapping factors in the subcarriers. By doing so, it was possible to fit the NB-IoT signal into the electrical bandwidth of the VLC transmitter, which is notably low-pass limited, particularly when using high-power low-cost PC-LEDs. Since the VLC channel, which spans from the LED to the Photodetector, uses
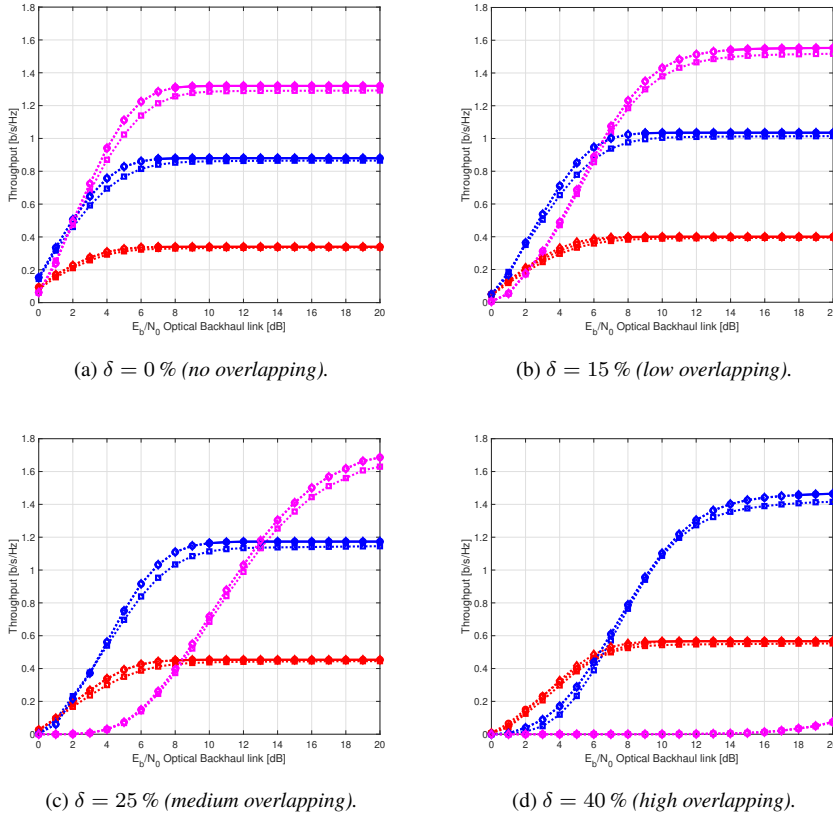
(a) $\delta = 0\,\%$ *(no overlapping)*.

(b) $\delta = 15\,\%$ *(low overlapping)*.

(c) $\delta = 25\,\%$ *(medium overlapping)*.

(d) $\delta = 40\,\%$ *(high overlapping)*.

Fig. 7: *End-to-end normalized throughput versus E_{b}/N_0 in the backhaul link for a NB-IoT frame with Detect-and-Forward relaying (SNR$_{\mathrm{al}}$ = 15 dB). NB-IoT code rates: 0.17 (red), 0.44 (blue), 0.67 (magenta). The UAV altitudes are 10 m (square marker), 30 m (circle marker), and 100 m (diamond maker). Solid (dashed) lines with (un)filled markers: BLER 10^{-2} requirement (not) fulfilled.*

an IM/DD transmission scheme, the multi-carrier non-orthogonal waveform (NSC-FDMA) of the optical backhaul link must be represented by real-valued samples that are suitable to modulate the light intensity of the LED. To fulfill this requirement, it was shown that the NSC-FDMA waveform had to verify the Hermitian Symmetric constraint and rotate the phase of its output.

Extensive simulations were carried out, which showed that *Decode-and-Forward* relaying offers a better BLER performance than the *Detect-and-Forward* scheme. In particular, when using the *Detect-and-Forward* relaying architecture at an equivalent E_{b}/N_0 in the optical backhaul link that was higher than 14 dB, the non-frequency-packed schemes offered a throughput gain of about 18%. For the *Decode-and-Forward* relaying, the maximum throughput gain was achieved when the E_{b}/N_0 in the radio

(a) $\delta = 0\,\%$ *(no overlapping).*

(b) $\delta = 15\,\%$ *(low overlapping).*

(c) $\delta = 25\,\%$ *(medium overlapping).*

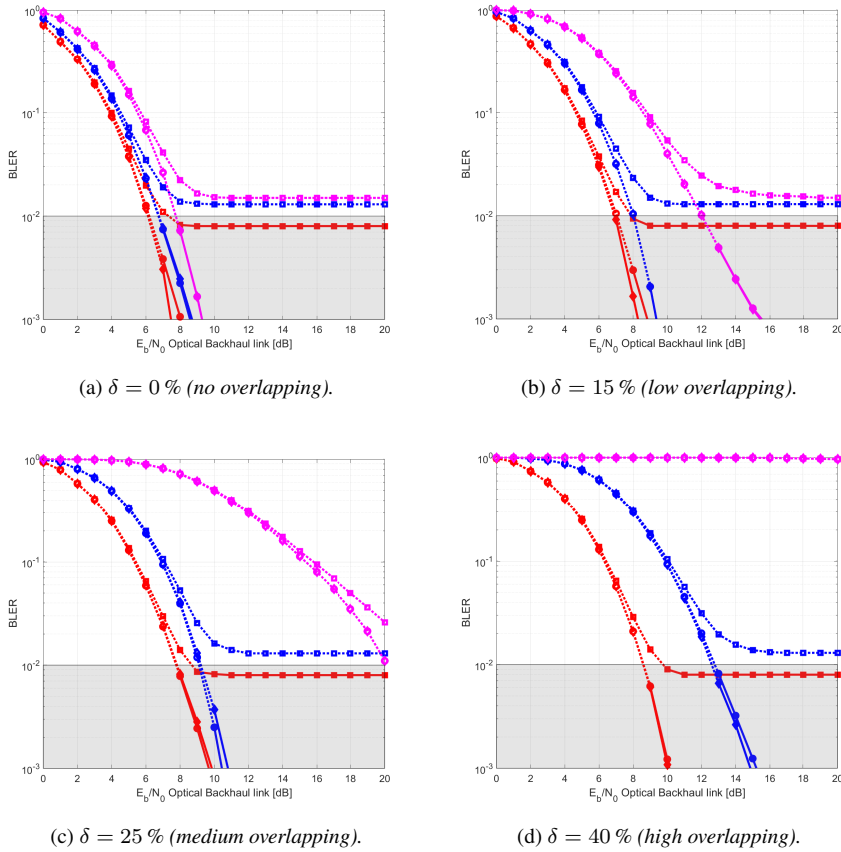(d) $\delta = 40\,\%$ *(high overlapping).*

Fig. 8: *End-to-end BLER versus equivalent E_b/N_0 in the backhaul link for a NB-IoT frame with Decode-and-Forward relaying ($SNR_{al} = 15\,dB$). NB-IoT code rates: 0.17 (red), 0.44 (blue), 0.67 (magenta). The UAV altitudes are $10\,m$ (square marker), $30\,m$ (circle marker), and $100\,m$ (diamond maker). Solid (dashed) lines with (un)filled markers: BLER 10^{-2} requirement (not) fulfilled.*

access link was $15\,\mathrm{dB}$. For this case, throughput gains between 32% and 68% were observed. Otherwise, throughput gains were reduced to about 18% when the equivalent E_b/N_0 of the optical backhaul was larger than $12\,\mathrm{dB}$.

The effect of the altitude of the UAV in the end-to-end performance was also studied in this paper. Since the statistics of the radio access channel gains at low UAV altitudes tended to be Rayleigh distributed, the best option in this situation was to implement a *Decode-and-Forward* relaying strategy. In contrast, for altitudes between 30 and $100\,\mathrm{m}$, the specular component of the Rician fading model gained importance, and the radio access channel started to become more Line-of-Sight distributed. Due to that, the BLER and throughput that were obtained for medium-to-high UAV altitudes were
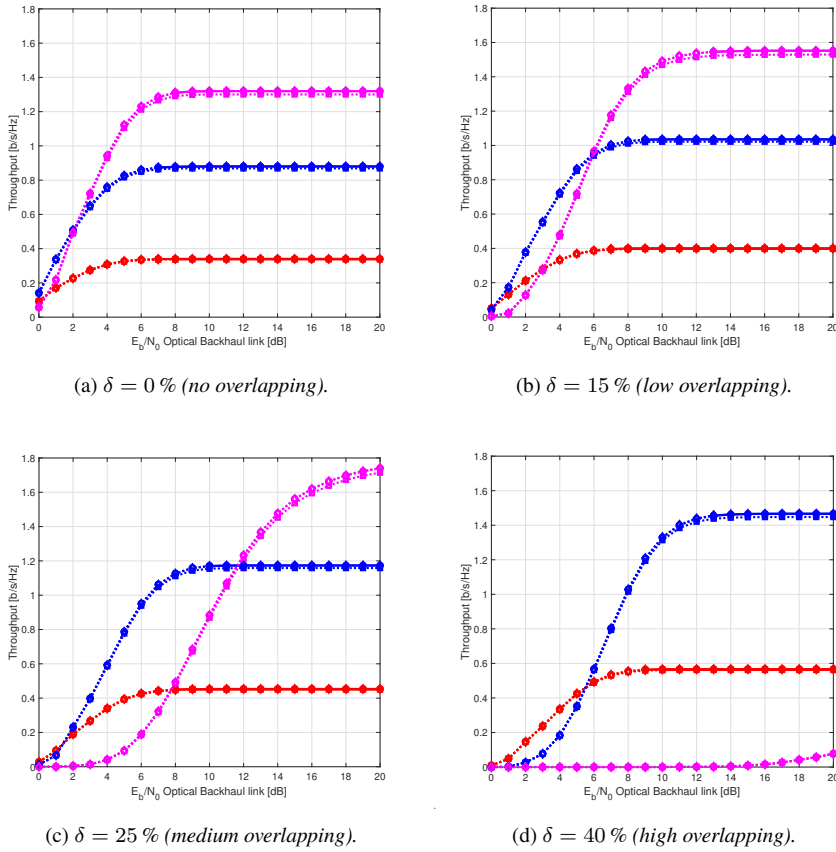
(a) $\delta = 0\%$ (no overlapping).

(b) $\delta = 15\%$ (low overlapping).

(c) $\delta = 25\%$ (medium overlapping).

(d) $\delta = 40\%$ (high overlapping).

Fig. 9: *End-to-end normalized throughput versus E_b/N_0 in the backhaul link for a NB-IoT frame in the Decode-and-Forward relaying ($SNR_{al} = 15\,dB$). NB-IoT code rates: 0.17 (red), 0.44 (blue), 0.67 (magenta). The UAV altitudes are $10\,m$ (square marker), $30\,m$ (circle marker), and $100\,m$ (diamond maker). Solid (dashed) lines with (un)filled markers: BLER 10^{-2} requirement (not) fulfilled.*

practically the same. In this situation, the *Decode-and-Forward* relaying strategy was able to provide the best throughput gain for low-to-medium equivalent E_b/N_0 values in the optical backhaul link. At large equivalent E_b/N_0 values (*i.e.*, beyond $14\,dB$), in contrast, both *Detect-and-Forward* and *Decode-and-Forward* relaying strategies offered practically the same performance in terms of throughput gain.

Regarding, the channel coding effect, it has been concluded that the higher the altitude of the UAV, the larger the channel coding rate and time-packing overlapping that can be used for the two proposed relaying strategies to meet the target BER. The reason is that if the altitude of UAV increases, then the channel has lower variation and so, the SNR improves. This conclusion holds for the two proposed relaying strategies.
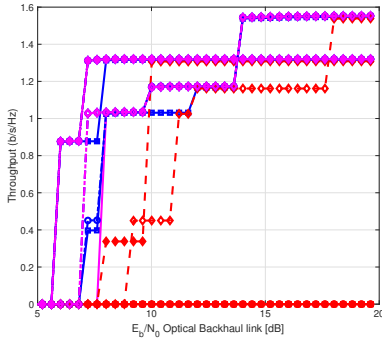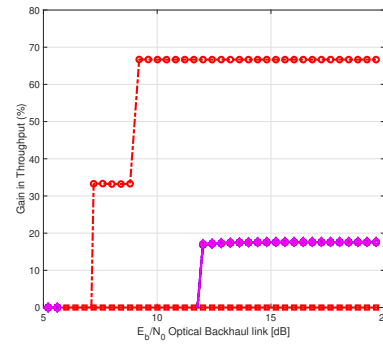
(a) *Envelope of the throughput for (non-)frequency-packing with Detect-and-Forward.*
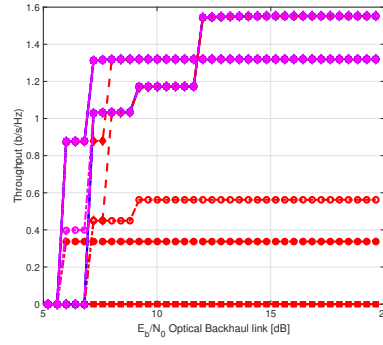
(b) *Envelope of the throughput for (non-)frequency-packing with Decode-and-Forward.*
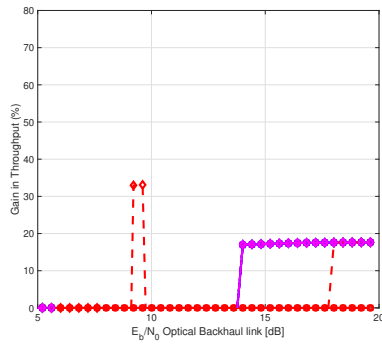
(c) *Gain in Throughput for Detect-and-Forward.*

(d) *Gain in Throughput Decode-and-Forward.*

Fig. 10: *End-to-end envelope of the normalized throughput and gain of frequency-packing schemes versus no-frequency-packing ones for different E_{b}/N_0 in the optical backhaul link. Left-hand side panels: Detect-and-Forward relaying. Right-hand side panels: Decode-and-Forward relaying. (Non-)filled markers: (Non-)frequency-packing schemes. For the radio access link, $E_{\mathrm{b}}/N_0 = 10\,dB$ (red marker), $15\,dB$ (blue marker), and $20\,dB$ (magenta marker). UAV altitudes: $10\,m$ (square marker), $30\,m$ (circle marker), and $100\,m$ (diamond marker).*

References

1. 3GPP, "3rd Generation Partnership Project; Technical Specification Group Radio Access Network; Study on New Radio (NR) to support non-terrestrial networks (Release 15)," Tech. Rep. TR 38.811, 2020. Rel. 15.

2. J. Aragón-Zavala, A.; Cuevas-Ruíz and J. Delgado-Penín, *High Altitude Platforms for Wireless Communications*. New York, NY, USA: Wiley, 2008.

3. W. e. a. Saad, *Wireless Communications and Networking for Unmanned Aerial Vehicles*. Cambridge, UK, 2020: Cambridge University Press, 2021.

4. A. T. Koubaa, *Unmanned Arial Systems. Theoretical Foundations and Applications*. Amsterdam, NE, 2021: Elsevier Academic Press, 2021.

5. M. Mozaffari, W. Saad, M. Bennis, Y.-H. Nam, and M. Debbah, "A tutorial on uavs for wireless networks: Applications, challenges, and open problems," *IEEE Communications Surveys Tutorials*, vol. 21, no. 3, pp. 2334–2360, 2019.

6. A. Al-Hourani, S. Kandeepan, and S. Lardner, "Optimal lap altitude for maximum coverage," *IEEE Wireless Communications Letters*, vol. 3, no. 6, pp. 569–572, 2014.

7. W. Saad, Z. Han, T. Basar, M. Debbah, and A. Hjorungnes, "A selfish approach to coalition formation among unmanned air vehicles in wireless networks," in *2009 International Conference on Game Theory for Networks*, pp. 259–267, 2009.

8. P. Zhan, K. Yu, and A. Lee Swindlehurst, "Wireless relay communications using an unmanned aerial vehicle," in *2006 IEEE 7th Workshop on Signal Processing Advances in Wireless Communications*, pp. 1–5, 2006.

9. F. Jiang and A. L. Swindlehurst, "Optimization of uav heading for the ground-to-air uplink," *IEEE Journal on Selected Areas in Communications*, vol. 30, no. 5, pp. 993–1005, 2012.

10. Y. Zeng, R. Zhang, and T. J. Lim, "Throughput maximization for uav-enabled mobile relaying systems," *IEEE Transactions on Communications*, vol. 64, no. 12, pp. 4983–4996, 2016.

11. Q. Wu, Y. Zeng, and R. Zhang, "Joint trajectory and communication design for multi-uav enabled wireless networks," *IEEE Transactions on Wireless Communications*, vol. 17, no. 3, pp. 2109–2121, 2018.

12. T. M. Cabreira, P. R. Ferreira, C. D. Franco, and G. C. Buttazzo, "Grid-based coverage path planning with minimum energy over irregular-shaped areas with uavs," in *2019 International Conference on Unmanned Aircraft Systems (ICUAS)*, pp. 758–767, 2019.

13. G. Yang, R. Dai, and Y.-C. Liang, "Energy-efficient uav backscatter communication with joint trajectory design and resource optimization," *IEEE Transactions on Wireless Communications*, vol. 20, no. 2, pp. 926–941, 2021.

14. W. Sun, "Distributed optimal scheduling in uav swarm network," in *2021 IEEE 18th Annual Consumer Communications Networking Conference (CCNC)*, pp. 1–4, 2021.

15. J. Lyu, Y. Zeng, and R. Zhang, "Cyclical multiple access in uav-aided communications: A throughput-delay tradeoff," *IEEE Wireless Communications Letters*, vol. 5, no. 6, pp. 600–603, 2016.

16. M. Mozaffari, W. Saad, M. Bennis, and M. Debbah, "Wireless communication using unmanned aerial vehicles (uavs): Optimal transport theory for hover time optimization," *IEEE Transactions on Wireless Communications*, vol. 16, no. 12, pp. 8052–8066, 2017.

17. J. Bas and A. Dowhuszko, "Indoor monitoring system based on arq signaling generated by a visible light communication link," *IEEE Globecom*, pp. 1–6, Dec. 2021.

18. E. A. S. Agency, "Easy access rules for unmanned aircraft systems," *European Union*, p. 312, 2021.

19. 3GPP, "LTE; Evolved Universal Terrestrial Radio Access (E-UTRA); Physical channels and modulation (3GPP TS 36.211 version 16.4.0 Release 16)," Tech. Rep. TS 36.211, 2021. Rel. 16.4.

20. Z. Li and C. Zhang, "An improved fd-dfe structure for downlink vlc systems based on sc-fdma," *IEEE Communications Letters*, vol. 22, no. 4, pp. 736–739, 2018.

21. 3GPP, "Technical Specification Group Radio Access Network; Evolved Universal Terrestrial Radio Access (E-UTRA); Multiplexing and channel coding," Tech. Rep. TS 36.212, 2021. Rel. 16.4.

22. 3GPP, "Enhanced lte support for aerial vehicles (Rel. 15)," *3GPP technical specification, TS 36.777, Ver. 15.0.0*, 2018.

23. C. B. Z. Qiu, C. Calvo-Ramirez and X. Yin, "Low altitude uav air-to-ground channel measurement and modeling in semiurban environments," *Hindawi Wireless Communications and Mobile Computing*, vol. 1, no. 1, pp. 1–11, 2017.

24. S. Shao, P. Hailes, T.-Y. Wang, J.-Y. Wu, R. G. Maunder, B. M. Al-Hashimi, and L. Hanzo, "Survey of turbo, ldpc, and polar decoder asic implementations," *IEEE Communications Surveys Tutorials*, vol. 21, no. 3, pp. 2309–2333, 2019.

25. Q. Wang, Q. Xie, Z. Wang, S. Chen, and L. Hanzo, "A universal low-complexity symbol-to-bit soft demapper," *IEEE Transactions on Vehicular Technology*, vol. 63, no. 1, pp. 119–130, 2014.

26. T. Komine and M. Nakagawa, "Fundamental analysis for visible-light communication system using LED lights," *IEEE Trans. Consumer Electronics*, vol. 50, pp. 100–107, Feb. 2004.

27. S. D. Dissanayake and J. Armstrong, "Comparison of aco-ofdm, dco-ofdm and ado-ofdm in im/dd systems," *Journal of Lightwave Technology*, vol. 31, no. 7, pp. 1063–1072, 2013.

28. J. Bas and A. Dowhuszko, "End-to-end error control coding capability of nb-iot transmissions in a geo satellite system with time-packed optical feeder link," *Industrial IoT Technologies and Applications*, April 2021.